Journal of Materials Chemistry C

ROYAL SOCIETY OF CHEMISTRY

PAPER

View Article Online
View Journal | View Issue

Cite this: J. Mater. Chem. C, 2023, 11, 6713

Critical evaluation of the thermometric performance of ratiometric luminescence thermometers based on $Ba_3(VO_4)_2$:Mn^{5+},Nd^{3+} for deep-tissue thermal imaging†

W. M. Piotrowski, *[a] R. Marin,[bc] M. Szymczak,[a] E. Martín Rodríguez,[de] D. H. Ortgies,[bce] P. Rodríguez-Sevilla,[be] P. Bolek,[f] M. D. Dramićanin,[g] D. Jaque[bce] and L. Marciniak *[a]

Near-infrared (NIR) luminescence thermometry has been brought to the fore as a reliable approach for remote thermal sensing and imaging. Lanthanide (Ln^{3+})-based nanophosphors are often proposed as NIR nanothermometers of choice. However, the combination of Ln^{3+} with transition metal (TM) ions has recently emerged as a strategy to introduce additional emission bands and/or TM ↔ Ln^{3+} energy transfer pathways whose temperature dependence can be harnessed to increase the sensitivity of the thermometric approach. Yet, the examples of the combination of luminescence nanothermometers working in the NIR and hosting simultaneously TM and Ln^{3+} are scarce, leaving plenty of space for the exploration of these systems. Herein, we report on the preparation and optimization of the thermometric performance of $Ba_3(VO_4)_2$:Mn^{5+},Nd^{3+} nanophosphors. The different temperature dependences of the emission intensity of the two doped luminescent centers allow using the ratio between Mn^{5+} and Nd^{3+} as a reliable thermometric parameter with a relative thermal sensitivity of 1% K^{-1} close to room temperature. We then showcase the suitability of this nanophosphor for employment in 2D NIR luminescence thermal imaging. Lastly, we critically evaluate the possibility of using this thermal imaging approach through opaque media with the help of phantoms with tissue-like optical properties. As expected, a loss of reliability of the thermometric method is observed due to tissue-induced photon scattering and absorption that differentially affect the emission of Mn^{5+} and Nd^{3+}. Overall, the reported results underscore the good performance of the newly developed nanothermometer, while consolidating the call for the use of luminescence nanothermometers working in the time-domain (rather than in the spectral domain) for deep-tissue thermal readout/imaging.

Received 20th January 2023,
Accepted 26th April 2023

DOI: 10.1039/d3tc00249g

rsc.li/materials-c

Introduction

Thermal sensing and thermal imaging with near-infrared (NIR) emitting luminescence thermometers are particularly appealing from a biological standpoint.[1–4] The ability to monitor the temperature of biological systems remotely and in a minimal invasive way has opened up new research avenues, allowing to obtain a better understanding of biological processes at the tissue and cellular levels, as well as the development of highly specific diagnostic tools.[5,6] Deep-tissue thermal imaging requires the use of phosphors with high luminescence brightness in the optical biological windows (750–950) (NIR-I), 1000–1350 nm (NIR-II), and 1500–1800 nm (NIR-III), wherein the scattering and absorption of light by tissues is reduced.[7,8]

One of the most reliable methods of measuring the temperature in luminescence thermometry is the ratiometric approach employing the ratio of the intensities of two emission

[a] Institute of Low Temperature and Structure Research, Polish Academy of Sciences, Okólna 2, 50-422 Wroclaw, Poland. E-mail: w.piotrowski@intibs.pl, l.marciniak@intibs.pl
[b] Nanomaterials for Bioimaging Group (nanoBIG), Departamento de Física de Materiales, Facultad de Ciencias, Universidad Autónoma de Madrid, C/Francisco Tomás y Valiente 7, 28049 Madrid, Spain
[c] Institute for Advanced Research in Chemistry (IAdChem), Campus de Cantoblanco, 28049 Madrid, Spain
[d] Nanomaterials for Bioimaging Group (nanoBIG), Departamento de Física Aplicada, Facultad de Ciencias, Universidad Autónoma de Madrid, C/Francisco Tomás y Valiente 7, 28049 Madrid, Spain
[e] Nanomaterials for Bioimaging Group (nanoBIG), Instituto Ramón y Cajal de Investigación Sanitaria (IRYCIS), Hospital Ramón y Cajal, Ctra. De Colmenar Viejo km 9.100, 28034 Madrid, Spain
[f] Faculty of Chemistry, University of Wrocław14 F. Joliot-Curie, Wrocław 50-383, Poland
[g] Centre of Excellence for Photoconversion, Vinča Institute of Nuclear Sciences – National Institute of the Republic of Serbia, University of Belgrade, P.O. Box 522, Belgrade 11001, Serbia

† Electronic supplementary information (ESI) available. See DOI: https://doi.org/10.1039/d3tc00249g

bands with different temperature-induced variations.[9–14] A significant difference in the thermal dependence of the two bands under consideration ensures a high measurement sensitivity in this approach. Co-doping transition metal (TM) ions and lanthanide (Ln^{3+}) ions in the same matrix, for example, provides such a possibility.[14–21] Temperature-induced luminescence quenching mechanisms differ depending on the configuration of the energy levels of both types of dopants.[22] With an appropriate ion selection, the Ln^{3+} signal (with less thermal variation) can be used as an internal luminescence reference.

In this vein, recent studies have pointed out at Mn^{5+} as an ideal TM for the preparation of luminescence thermometers based on TM and Ln^{3+}.[23–27] Indeed, its emission band in the NIR-II region is highly susceptible to thermal quenching. Its spectrally narrow emission also limits overlaps with the NIR emission of co-doped Ln^{3+}. This aspect allays the concerns over the loss of reliability of ratiometric luminescence thermometry arising from signal admixing. However, the literature on the thermometric performance of Mn^{5+}-based luminescence thermometers is scarce, and even fewer studies deal with thermal imaging using this class of phosphors.[23–27] Given the above, the goal of this work is to critically evaluate the sensing and thermal imaging potential of $Ba_3(VO_4)_2$:Mn^{5+}, Nd^{3+} based on the ratios of Mn^{5+} and Nd^{3+} ion intensities.

In this paper, we present an unprecedented $Ba_3(VO_4)_2$:Mn^{5+},Nd^{3+} luminescence thermometer. The luminescence intensity ratio (LIR) between Mn^{5+} and Nd^{3+} emissions provides a reliable thermometric parameter. Subsequently, the concentration of Nd^{3+} ions was optimized to maximize the thermal sensing capability of the developed material. Following this, 2D temperature imaging of a thermal gradient was performed through glass first and then through tissue phantoms, simulating the difficult situation encountered in *in vivo* thermal sensing. A critical evaluation of the performance of this ratiometric luminescence thermometry approach is provided, highlighting the difficulties that spectral-based methods inherently present.

Experimental

Materials and chemicals

$Ba_3(VO_4)_2$:1% Mn^{5+}, y% Nd^{3+} (y = 0.1; 0.2; 0.5; 1; 2; 5) nanocrystals were synthesised using a modified Pechini method.[28] The following materials were used as reagents without further purification: $Ba(NO_3)_2$ (99.999% purity, Alfa Aesar), NH_4VO_3 (99.999% purity, Alfa Aesar), $MnCl_2{\cdot}4H_2O$ (>99.0% purity, Sigma Aldrich), Nd_2O_3 (99.99% purity, Stanford Materials Corporation) and $C_6H_8O_7$ (>99.5% purity, Alfa Aesar). The starting materials were weighed so that the total amount of moles of metals was equal to 4.00×10^{-4} mol.

Nanocrystal preparation

Stoichiometric amounts of $Ba(NO_3)_2$, NH_4VO_3 and $MnCl_2{\cdot}4H_2O$ were dissolved in deionized water in separate glasses and then mixed together. Neodymium oxide was dissolved in deionized water with the addition of 2 mL of HNO_3 (65% purity, Avantor), then recrystallized three times to remove the excess HNO_3 and added to the aqueous solution of other reagents. After this, 24.0×10^{-4} mol of anhydrous citric acid was added to the mixture with the molar ratio of citric acid at all metals set to 6 : 1. Subsequently, the samples with a concentration of 0.1% Mn^{5+} with respect to the number of V^{5+} ions and y% Nd^{3+} in relation to the number of Ba^{2+} ions were calcined in porcelain crucibles at 1000 °C in air for 8 h. Finally, the obtained powders were ground using an agate mortar.

Tissue phantom preparation

Tissue phantoms were prepared based on a modified procedure described in ref. 29. In this work, two types of phantom tissues were used, consisting of 50% intralipids emulsion (tissue phantom A), and 50% intralipids emulsion with 0.1% of Indian ink (tissue phantom B). For this purpose, the intralipids emulsion (20% in water, Sigma Aldrich) and deionized water in a 1 : 1 ratio were added into a 100 mL Erlenmeyer flask to achieve a final volume of 50 mL. The mixture was placed in an oil bath, preheated at 363 K and kept under stirring (350 rpm). When considering tissue phantom B, 0.1% Indian ink was added at this stage. Next, 2%wt of agar powder was added and left under stirring at 363 K for 30 minutes until the agar was completely dissolved. After this time, the mixture was poured into a crystallizing dish and allowed to cool down to room temperature until the gel sets. All gels of 1.3 mm in thickness were stored in the fridge for further use.

Characterization

All synthesized materials were examined by X-ray powder diffraction (XRPD) measurements using a PANalitycal X'Pert diffractometer, equipped with an Anton Paar TCU 1000 N temperature control unit, using Ni-filtered Cu K_α radiation (V = 40 kV, I = 30 mA).

Transmission electron microscopy (TEM) images were taken using an FEI TECNAI G2 X-TWIN microscope. The powders were dispersed in methanol with the aid of ultrasounds and deposited on lacey-type copper grids. The studies were performed with 300 keV parallel beam electron energy. The images were digitally recorded using a Gatan Ultrascan 1000XP.

The emission spectra were recorded using the 808 nm excitation lines from a laser diode (Changchun New Industries Optoelectronics Technology Co. Ltd) and a NIRQUEST spectrometer from Ocean Optics (1.5 nm spectral resolution) as a detector. The excitation spectra and luminescence decay profiles were recorded using an FLS1000 fluorescence spectrometer from Edinburgh Instruments with a R5509-72 photomultiplier tube from Hamamatsu in nitrogen-flow cooled housing as a detector with a 450 W halogen lamp and a 668 nm pulsed work laser diode (Changchun New Industries Optoelectronics Technology Co. Ltd) as excitation sources. The low-temperature emission spectra were also obtained using an FLS1000 fluorescence spectrometer. The temperature of the sample was controlled using a THMS 600 heating-cooling stage from Linkam (0.1 K temperature stability and 0.1 K set point resolution).

The quantitative composition of $Ba_3(VO_4)_2$:0.1% Mn^{5+}, y% Nd^{3+} (y = 0.1, 0.2, 0.5, 1, 2, and 5) nanocrystals was determined using inductively coupled plasma atomic emission spectroscopy (ICP-AES). ICP-OES analysis was carried out using an iCAP 7400 DUO ICP-OES Thermo Scientific spectrometer equipped with a high-performance solid-state Charge Injection Device (CID) detector, the CID86, enabling the free choice of wavelengths over the 166–847 nm range. The experimental data were collected using Qtegra ISDS software. For measurements, all the powders of $Ba_3(VO_4)_2$: Mn^{5+},Nd^{3+} were dissolved in 65% HNO_3.

For imaging experiments, the sample was placed in an optical setup especially designed for fluorescence imaging in NIR-II: the PhotonSWIR Imager from BioSpace Lab (Nesles-la-Vallée, France). An InGaAs CCD camera (WiDy SenS 640V-ST, New Imaging Technologies, France) with a fiber-coupled 808 nm laser diode (LIMO) and two filters placed in an automatic filter wheel, namely a 1200 nm bandpass filter (Edmund Optics, Techspec OD4.0 25 nm Bandpass Filter FWHM = 25 nm) and a 1150 nm shortpass filter (Edmund Optics, Techspec OD2.0 Short-pass Filter), are the main components. Additionally, the camera is always protected using an 850 nm long-pass filter (Thorlabs, FEL850). For the first experiment without the presence of tissue phantoms and the second with tissue phantom A, the laser was set to a maximum output power of 14.1 mW and collected by a lens for the illumination of the samples with a maximum (peak) power density of 0.05 mW cm^{-2}. For measurements *via* tissue phantom B, the maximum output power of the laser was set to 53.9 mW, resulting in a maximum power density of 0.21 mW cm^{-2}. The materials were illuminated with a laser diode in a continuous mode, and the system was operated in a ratiometric mode taking 25 image pairs with 0.5 s exposure time for each image and the automatic filter change taking 0.1 s in between, followed by a pause of 1 s before repeating the sequence with the next pair.

Results and discussion

Structural and morphological characterization

The rhombohedral structure of $Ba_3(VO_4)_2$ (with $R\bar{3}m$ space group) consists of $(VO_4)^{3-}$ tetrahedra and Ba^{2+} cations coordinated by 6 or 10 O^{2-} anions (Fig. 1(a)).[30–34] When considering doping of the structure with manganese ions, it is expected that they will occupy V^{5+} sites due to the small difference in the effective ionic radii of Mn^{5+} and V^{5+} at the tetrahedral site (33.0 and 35.5 pm, respectively) and similarity in the ionic charge. On the other hand, co-doping with Nd^{3+} ions is possible due to their occupation of the crystallographic sites of Ba^{2+}. Due to the lack of a reported value for the ionic radius of Nd^{3+} at the 10-fold coordinated site, it can be assumed that the Nd^{3+} ions preferentially substitute Ba^{2+} at the octahedral sites. This is also expected due to the smaller difference between the ionic radii of Nd^{3+} and Ba^{2+} located at the 6-fold coordinated site than with that located at the 10-fold coordinated sites (98,3, 142 and 152 pm, respectively). However, it should be noted that there is a charge mismatch between the Nd^{3+} and Ba^{2+} ions, which will generate additional defects, and the high concentration can lead to significant changes in the structure of the vanadate along with a high number of optical traps. To verify

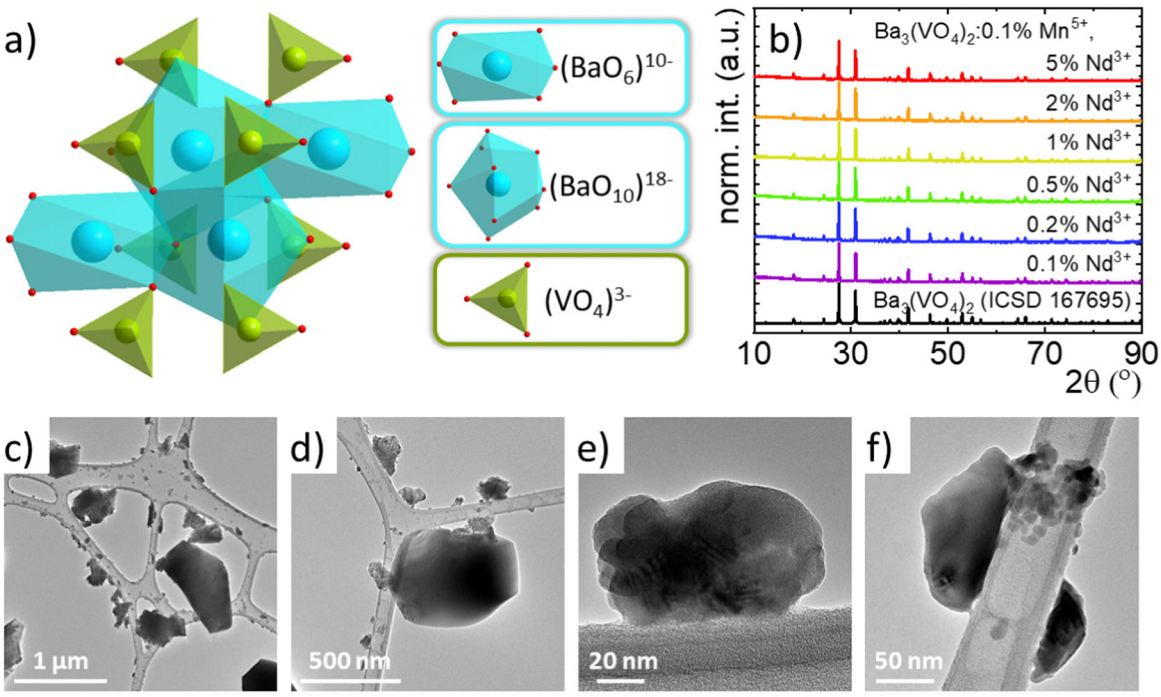

Fig. 1 Structural characterization of synthesized materials: the crystal structure of the $Ba_3(VO_4)_2$ unit cell (a). X-ray diffraction patterns of $Ba_3(VO_4)_2$:0.1% Mn^{5+} co-doped with different Nd^{3+} concentrations (b). Representative TEM images of $Ba_3(VO_4)_2$:0.1% Mn^{5+}, 0.1% Nd^{3+} materials (c)–(f).

whether the concentration of Nd^{3+} ions affects the crystallographic structure of the synthesized $Ba_3(VO_4)_2$ nanocrystals, the XRPD patterns were analyzed (Fig. 1(b)). A previous work showed that the diffraction reflection of $Ba_3(VO_4)_2$ doped with 0.1% Mn^{5+} corresponds to the reference pattern (ICSD 167695) confirming the phase purity of the synthesized phosphors. Furthermore, co-doping with Nd^{3+} ions with concentrations in the range of 0.1% to 5% also does not lead to the formation of an additional crystalline phase.

Transmission electron microscopy (TEM) studies of $Ba_3(VO_4)_2$: 0.1% Mn^{5+} co-doped with Nd^{3+} ions are also in agreement with previous studies for materials singly doped with Mn^{5+} ions.[25] It can be concluded that the particles are well crystallized with a tendency to agglomerate (Fig. 1(c)–(f) and Fig. S1, ESI†). The particle size distribution determined by Feret's method suggests that more than 90% of the observed particles are smaller than 100 nm (Fig. S2, ESI†). For materials co-doped with 0.1% Nd^{3+}, the average particle size is estimated to be 65 nm, while when the Nd^{3+} concentration increases to 5%, the particle size increases to 84 nm. However, some sub-microcrystalline particles can be found in the samples. This observation is in agreement with the average particle sizes of $Ba_3(VO_4)_2$:0.01% Mn^{5+} and $Ba_3(VO_4)_2$:0.01% Mn^{5+}, 2% Er^{3+} previously reported with 52 nm and 72 nm in size, respectively. It also confirms the previously suggested effect of the Ln^{3+} ion concentration on the increasing size of the particles. The results of the analysis of the chemical composition of the samples (ICP) are presented in Table S1 (ESI†) and are in agreement with the stoichiometric amounts used for the synthesis.

Characterization of luminescence properties

To understand the spectroscopic properties of the Mn^{5+}/Nd^{3+} co-doped system, the simplified configurational coordinate diagram of Mn^{5+} with the energy diagram of Nd^{3+} is shown in Fig. 2(a). In the excitation spectra of the $Ba_3(VO_4)_2$:Mn^{5+},Nd^{3+} nanocrystals, two broad absorption bands can be found with the maxima at around 370 and 700 nm. The most intense latter one corresponds to the electronic transition from the $^3A_2$ ground state to the $^3T_2$ excited state. Since λ_{exc} = 808 nm is a relatively inexpensive light source, matches with the $^3A_2 \rightarrow {}^3T_2$ absorption band, and falls within the NIR-I spectral range, it was used as an excitation source in this work. The population of the excited state is followed by a non-radiative depopulation to the excited emitting state ^1E. The $^1E \rightarrow {}^3A_2$ radiative transition leads to the generation of the narrow emission band at approximately 1180 nm. As already proved,[16] the most sensitive optical response in the case of the TM/Ln^{3+} co-doped luminescence thermometers can be achieved when the employed irradiation excites independently both TM and Ln^{3+}. This is because when the TM $\rightarrow$ Ln^{3+} energy transfer is responsible for the population of the excited state of Ln^{3+}, it affects its luminescence thermal stability and thus lowers the sensitivity of the luminescence thermometer. In this sense, Nd^{3+} is a promising candidate since its intense absorption band corresponding to the $^4I_{9/2} \rightarrow {}^4F_{5/2}$, $^2H_{9/2}$ transition overlaps with the 808 nm excitation chosen for this study. Upon this excitation, the $^4F_{5/2}$, $^2H_{9/2}$ state is populated and its nonradiative depopulation causes the occupation of the $^4F_{3/2}$ metastable state. As a result of the radiative depopulation of the metastable state,

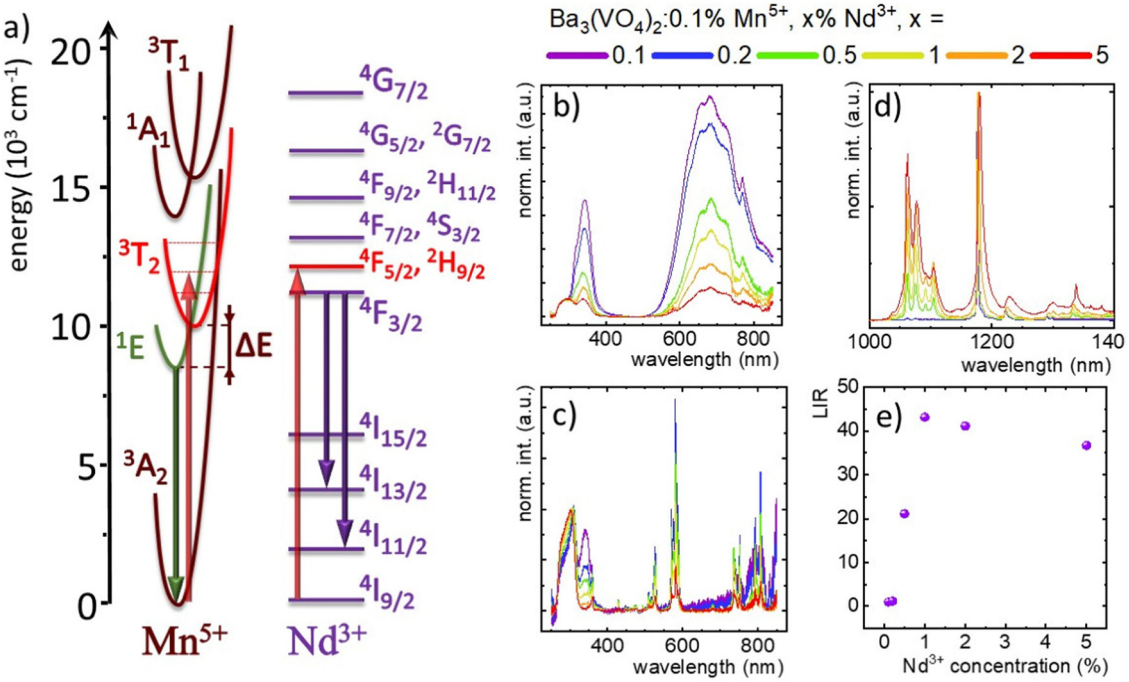

Fig. 2 Configurational coordinate diagram for Mn^{5+} and Nd^{3+} ions (a). Comparison of the low-temperature (83 K) excitation monitored at Mn^{5+} emission (λ_{em} = 1177 nm) (b) and at Nd^{3+} emission (λ_{em} = 1062 nm) (c). Emission spectra (λ_{exc} = 808 nm) of $Ba_3(VO_4)_2$:0.1% Mn^{5+} co-doped with different Nd^{3+} concentrations (d). Influence of the Mn^{5+} concentration on the LIR parameter (e).

three emission bands occur at 880, 1060, and 1350 nm corresponding to the $^4F_{3/2} \rightarrow {}^4I_{9/2}$, $^4F_{3/2} \rightarrow {}^4I_{11/2}$ and $^4F_{3/2} \rightarrow {}^4I_{13/2}$ electronic transitions, respectively.

To evaluate the theoretical assumptions and verify the existence of potential energy transfers between Nd^{3+} and Mn^{5+} ions, the excitation spectra recorded at 83 K were analyzed (Fig. 2(b)). In the case of the excitation spectra of Nd^{3+} ions monitored at λ_{em} = 1062 nm, numerous narrow bands have been noted which can be assigned to the transitions from the $^4I_{9/2}$ level to the $^4F_{3/2}$ (839 nm), $^4F_{5/2}$, $^2H_{9/2}$ (806.5 nm), $^4F_{7/2}$, $^4S_{3/2}$ (751 nm), $^4F_{9/2}$, $^2H_{11/2}$ (680 nm), $^4G_{5/2}$ (580 nm), $^2G_{7/2}$ (575 nm), $^4G_{7/2}$ (526.5 nm), $^2K_{13/2}$, $^4G_{9/2}$, $^2K_{13/2}$ (510 nm), $^2G_{9/2}$ (476.5 nm), $^2K_{15/2}$, $^4G_{11/2}$ (448 nm), $^2P_{1/2}$ (429.5 nm), $^4D_{3/2}$, $^4D_{5/2}$ (358.5 nm) and $^4D_{1/2}$ (347 nm) states. Furthermore, the spectra show two broad overlapped bands with maxima at 340 nm and ~305 nm that come from the charge transfer from the $(VO_4)^{3-}$ group.[25,30] The band centered at 340 nm decreases markedly compared to the band at ~305 nm as the concentration of Mn^{5+} increases, while the maximum of the second band gradually shifts from 312 nm to 301 nm for the phosphor doped with 0.1% and 5% of Mn^{5+} ions. This may be related to the gradual decrease in the strength of the crystal field that interacts with the $(VO_4)^{3-}$ group resulting from the substitution of larger Ba^{2+} ions with smaller Nd^{3+} ions. Due to the absence of additional bands in the excitation spectrum of Nd^{3+}, the energy transfer from Mn^{5+} to Nd^{3+} was excluded. A different shape is presented by the excitation spectrum of Mn^{5+} recorded at λ_{em} = 1177 nm at 83 K (Fig. 2(c)). It consists of broad excitation bands of Mn^{5+} ions originating from electron transitions $^3A_2 \rightarrow {}^1A_1$ (772 nm) and $^3A_2 \rightarrow {}^3T_1(^3F)$ (the broadband from 590 to 750 nm with a maximum at ~684 nm), as well as two bands associated with the charge transfer of the $(VO_4)^{3-}$ group centered at 344 nm and 300 nm. In the case of the Nd^{3+} excitation spectra, there was a marked decrease in the intensity of the band at 344 nm and its shift from 344 nm to 340 nm as the concentration of Nd^{3+} ions increased compared to the band at 300 nm. It is noteworthy that for the Nd^{3+} concentration above 1% additional narrow bands are observed, among others, around 805 nm 582 nm, and 575 nm, corresponding to the previously described Nd^{3+} absorption bands. This result confirms the $Nd^{3+} \rightarrow Mn^{5+}$ energy transfer for higher dopant concentrations. The independence of the simultaneous excitation of both Mn^{5+} and Nd^{3+} was confirmed by the analysis of the emission spectra of $Ba_3(VO_4)_2$:Mn^{5+},Nd^{3+} upon excitation at 808 nm. Even for low Nd^{3+} concentrations three emission bands at 1060, 1180 nm and 1350 nm can be observed (Fig. 2(d)). For higher Nd^{3+} concentrations, a small spectral shift of the Mn^{5+} band maximum occurs from 1174 to 1180 nm. This shift likely stems from an increased crystal field strength affecting the Mn^{5+} sites with a growing number of Nd^{3+} ions and it is related to a smaller ionic radius of the dopant with respect to Ba^{2+} ions. A unique feature of Mn^{5+} compared to other TM ions is its extremely narrow FWHM of 2.2 nm for the sample with 0.1% Nd^{3+} ions. The FWHM value gradually increases up to ~8.7 nm for $Ba_3(VO_4)_2$:0.1% Mn^{5+}, 5% Nd^{3+}, which may be related to the formation of additional asymmetries in the tetrahedral site of Mn^{5+} ions due to defects introduced by the electronic charge mismatch between Ba^{2+} and Nd^{3+} ions. Besides, vibronic sidebands of Mn^{5+} ions at 1168.8 nm, 1222.2 nm and 1291.3 nm can be noted. For nanocrystals doped with 0.1% and 0.2% Nd^{3+}, weak bands at 1075 nm and 1062 nm corresponding to the Stark levels of the $^4F_{3/2} \rightarrow {}^4I_{11/2}$ transition are also detectable. Interestingly, above 0.5% Nd^{3+}, these bands become more intense comparing the spectra normalized to the Mn^{5+} band maximum, and additional bands at 1330 nm associated with the $^4F_{3/2} \rightarrow {}^4I_{13/2}$ transition and additional Stark sublevels of the $^4F_{3/2} \rightarrow {}^4I_{11/2}$ transition at 1105 nm and 1092 nm appear.

To quantify the increase in the emission intensity of Nd^{3+} ions with respect to Mn^{5+} emission, the luminescence intensity ratio (LIR) parameter was introduced according to equation (eqn (1)):

$$\mathrm{LIR} = \frac{\int_{1057\ \mathrm{nm}}^{1077\ \mathrm{nm}} I\left(^4F_{3/2} \rightarrow {}^4I_{11/2}\right)\left[Nd^{3+}\right]d\lambda}{\int_{1168\ \mathrm{nm}}^{1195\ \mathrm{nm}} I\left(^1E \rightarrow {}^3A_2\right)[Mn^{5+}]d\lambda} \quad (1)$$

The LIR value normalized to the value obtained for 0.1% Mn^{5+}, 0.1% Nd^{3+} plotted as a function of the Nd^{3+} concentration (Fig. 2(e)) showed a value of 20 at 0.5% Nd^{3+}, reaching a maximum of 43 for 1% Nd^{3+}, before slightly decreasing to 37 for 5% Nd^{3+}. This trend at higher concentrations is probably associated with the reduction of the Nd^{3+} emission intensity *via* the $\{^4F_{3/2}, {}^4I_{9/2}\} \leftrightarrow \{^4I_{15/2}, {}^4I_{15/2}\}$ cross-relaxation process. The concentration quenching of the intensity of the Nd^{3+} emission is confirmed by the emission spectra recorded for $Ba_3(VO_4)_2$ co-doped with 1% Mn^{5+} and various concentrations of Nd^{3+} ions (in the range of 0.1% to 10%), where Nd^{3+} luminescence could not be observed (Fig. S3, ESI†).

Thermometric properties of the Mn^{5+}/Nd^{3+} co-doped system

The thermal dependence of a series of materials doped with 0.1% Mn^{5+} and different concentrations of Nd^{3+} ions was analyzed (Fig. 3(a) and Fig. S4–S6, ESI†). In the case of low Nd^{3+} concentrations, the Mn^{5+} intensity initially increases up to around 210 K followed by the decrease in the intensity. Hence, T_{50} (temperature at which the emission intensity reached half of its initial intensity at low temperature) is higher for the Mn^{5+}, 0.1–1%Nd^{3+} co-doped samples (T_{50} ~ 380–390 K) compared to the solely Mn^{5+} doped counterpart. Further increases in the Nd^{3+} concentration hamper the initial enhancement of emission intensity and thus T_{50} decreases to 270 K for 2%. This initial increase in the emission intensity was already reported for materials doped with Cr^{3+} and Mn^{4+} ions and was explained in terms of the overlap of the wave functions of two states and thus thermal increases in the probability of the radiative depopulation of the emitting state.[35–39] On the other hand, the Nd^{3+}emission intensity was expected to be affected to a lower extent by temperature changes (Fig. 3(c)). For 0.1% Nd^{3+}, a slight increase in intensity was observed up to 423 K. Due to the low emission intensity of the Nd^{3+} ion for low dopant concentrations, the integral emission intensity may be affected by the strong contribution of the Mn^{5+} emission intensity. For a higher amount of dopant (0.5% and 1% Nd^{3+}), the monotonic

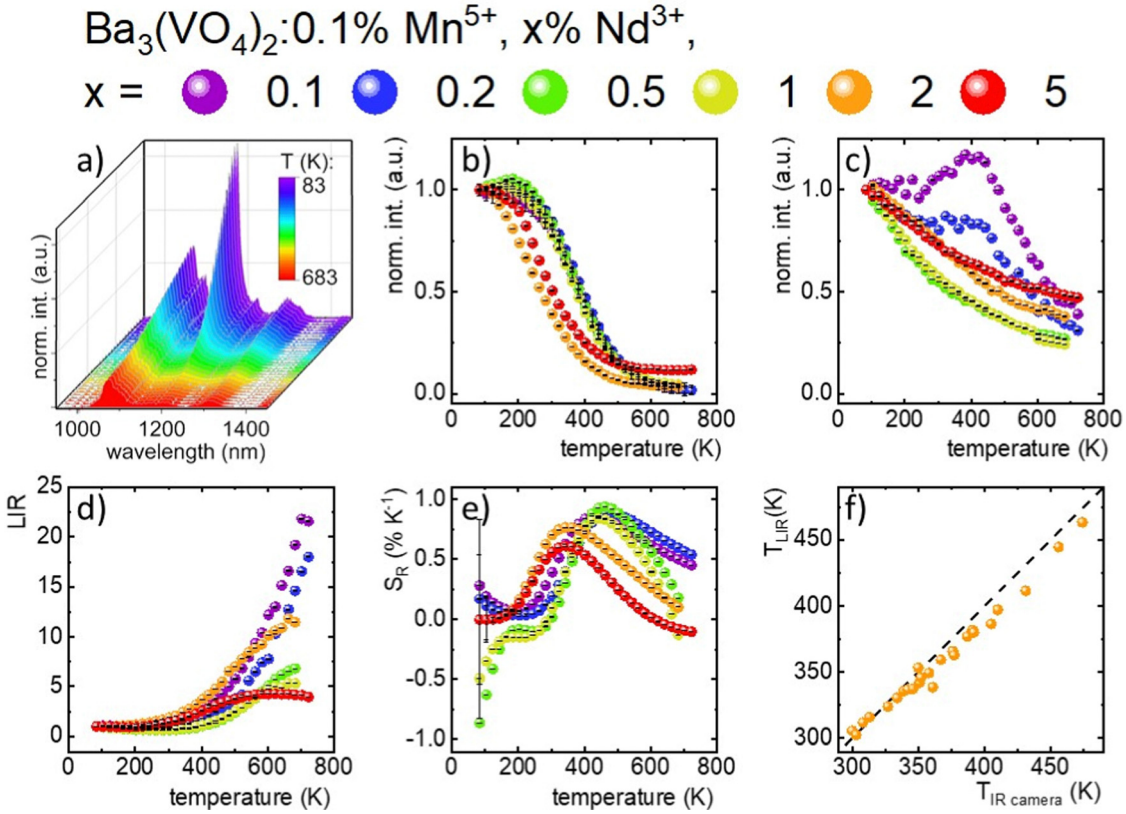

Fig. 3 Thermal evolution of the emission spectra of $Ba_3(VO_4)_2$:0.1% Mn^{5+}, 2% Nd^{3+} phosphor (a). Thermal evolution of the Mn^{5+} band intensity (b), Nd^{3+}band intensity (c), LIR (d) and S_R of $Ba_3(VO_4)_2$:0.1% Mn^{5+} co-doped with different concentrations of Nd^{3+} (e). Comparison of temperature calculated with LIR and temperature detected using an IR camera using $Ba_3(VO_4)_2$:0.1% Mn^{5+}, 2% Nd^{3+} – (f).

decreases of emission intensity at elevated temperatures up to 25% at 683 K was found. Nevertheless, Nd^{3+} was found to be significantly less susceptible to thermal changes with respect to Mn^{5+}, which enables the development of a luminescence thermometer based on the ratio of their emission intensities (Fig. 3(d)). The LIR value for 0.1% Mn^{5+}, 0.1% Nd^{3+} co-doped nanocrystals in the 83–243 K temperature range remains almost unchanged. Above 243 K, the quasi-exponential increase in the LIR value up to 22.0 at 703 K can be observed. Interestingly, when the concentration of Nd^{3+} increases, some saturation or even a decrease in the thermal dependence of LIR can be found. The temperature at which the reversion of the LIR monotonicity can be observed decreases with the dopant concentration from 690 K for 0.5% Nd^{3+} to 580 K for 5% Nd^{3+}. This is expected since at high temperatures the emission intensity of Mn^{5+} is almost completely quenched and the thermal change of the Nd^{3+} emission intensity reversed the thermal variation of the LIR. To verify the influence of the Mn^{5+} concentration on the thermal changes of the LIR values quantitatively, the relative sensitivity S_R was calculated according to the following formula (eqn (2)):

$$S_R = \frac{1}{LIR}\frac{\Delta LIR}{\Delta T} \times 100\% \quad (2)$$

where ΔLIR represents the change of LIR for the ΔT change of temperature. The obtained S_R results are plotted in Fig. 3(e). For 0.1% Nd^{3+}, the maximum sensitivity S_{Rmax} of about 0.83% K^{-1} was obtained at ~433 K, with S_R = ~0.40% K^{-1} at 303 K. For 0.2% Nd^{3+}, the value of S_{Rmax} = 0.88% K^{-1} was obtained at the highest temperature among the analyzed materials, *i.e.*, ~483 K. For higher concentrations of Nd^{3+} ions, a gradual shift in $T(S_{Rmax})$ toward lower temperatures was observed. The highest sensitivity value was obtained for 0.5% Nd^{3+}, which was equal to S_{Rmax} = 0.94% K^{-1} at 453 K. The highest S_R ~0.69% K^{-1} in the physiological temperature range was featured by the $Ba_3(VO_4)_2$:0.1% Mn^{5+}, 2% Nd^{3+} sample.

To verify the applicative potential of $Ba_3(VO_4)_2$:0.1% Mn^{5+}, 2% Nd^{3+} as a luminescence thermometer, an experiment with light-induced heating while simultaneously obtaining a thermal readout was performed. The excitation power density at λ_{exc} = 808 nm was changed and the luminescence spectra of Mn^{5+} and Nd^{3+} were recorded. In addition, the temperature of the sample was controlled by using an infrared thermometric camera. As can be seen, the increase in the excitation density results in the increase in the intensity of the Nd^{3+} emission, as expected (Fig. S7, ESI†). On the other hand, the emission intensity of Mn^{5+} ions decreases at a lower rate compared to the previously described experiments (Fig. 3(a)). This stems from the fact that luminescence thermal quenching competes with the increase of the emission intensity associated with the increase in the excitation density. The comparison of the

temperature determined using a thermal camera with the temperature determined by luminescence thermometry (LIR) in Fig. 3(f) reveals a very good agreement in the 300–450 K temperature range. This result confirms the high application potential of $Ba_3(VO_4)_2$:0.1% Mn^{5+}, 2% Nd^{3+} for temperature sensing.

Thermal imaging based on Mn^{5+} and Nd^{3+} ratios

Promising temperature sensing results based on LIR of Mn^{5+} and Nd^{3+} prompted the testing of the developed material's thermal imaging prowess and the corresponding thermometric approach. Fig. S10 (ESI†) shows a schematic representation of the measurement system, which includes a laser diode with an 808 nm excitation line, an NIR spectral camera, and a thermal camera. The phosphor powder was introduced between two glass microscope slides and one edge of the slide was placed in contact with a cold source. By heating the other edge of the glass slide, a temperature gradient was created. In order to provide ratiometric readout, the 2D images of luminescence were taken using alternately two optical filters *i.e.* a 1200 nm bandpass filter with a FWHM of 25 nm (for Mn^{5+} luminescence) and a 1150 nm shortpass filter (for Nd^{3+}) integrated in neighboring positions in an automated filter wheel. Representative intensity maps recorded during this experiment are shown in Fig. 4(a) (Mn^{5+}) and 4b (Nd^{3+}). Near the cooling area the intensity values of both images are similar. However, as the heating source was applied, the intensity in both maps decreased, but at a faster rate for the map in Fig. 4(a). This difference is

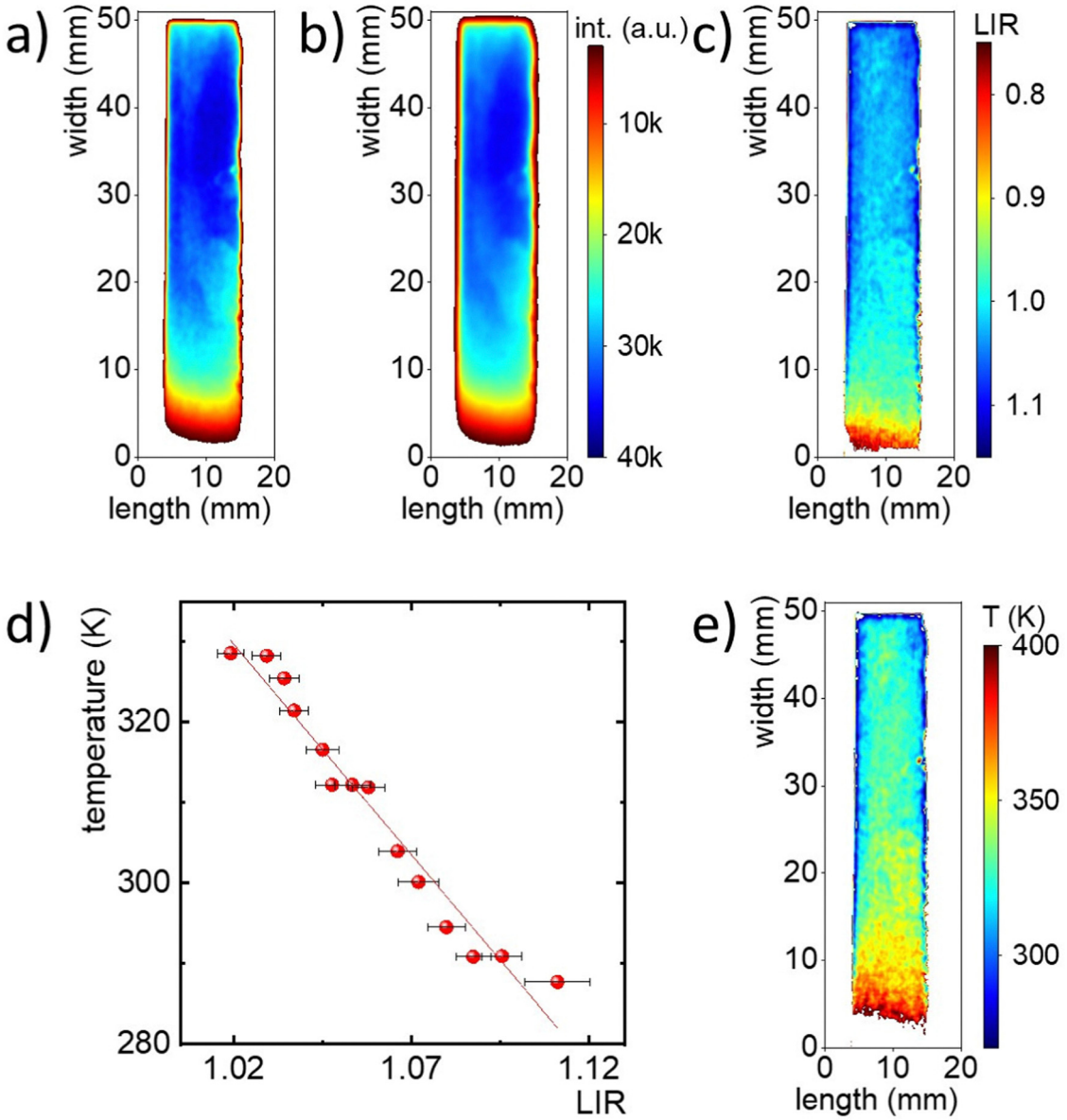

Fig. 4 The proof of concept experiment with an induced temperature gradient for $Ba_3(VO_4)_2$:0.1% Mn^{5+}, 2% Nd^{3+} phosphor: the intensity map with a 1200 nm bandpass filter (a) and 1150 nm shortpass filter (b). The LIR map (c). The calibration curve of temperature *vs.* LIR (d) and the calculated temperature map (f).

manifested in the LIR map, obtained by dividing the image taken using the 1200 nm bandpass filter by the image taken using the 1150 nm shortpass filter (Fig. 4(c)). The change in LIR values as a function of distance from the heating source can be clearly observed. It should be noted that lower LIR values were obtained near the heating source, indicating an inverse relationship with the temperature gradient. Yet, to obtain a temperature map from the LIR values, it was necessary to perform a calibration curve (Fig. 4(d)). Therefore, a series of measurements at predetermined constant temperatures of a heating plate were carried out. The resultant intensity images obtained for the two ions (Mn^{5+} and Nd^{3+}) were divided by each other to obtain the LIR images. Finally, a linear equation was used to convert the LIR map into a temperature map, as shown in Fig. 4(e). The resulting map shows the temperature gradient that covers a range of about 280–400 K, which agrees with the temperature gradient obtained from the thermal camera (Fig. S11, ESI†).

Ratiometric thermal imaging through tissue phantoms

Since the spectral range of the Mn^{5+} and Nd^{3+} emissions fall within the NIR-II spectral range, one would consider $Ba_3(VO_4)_2$: 0.1% Mn^{5+}, 2% Nd^{3+} suitable for through-tissue imaging and thermal sensing. To test this capability, the thermal mapping performance was further evaluated through tissue phantoms with different compositions (A and B, respectively without and with ink, alongside intralipids). The phantom composition was selected to study the effect of intralipid concentration, which mainly enhanced the scattering properties and Indian ink, which was responsible for improving the absorption properties on the total extinction properties. In each case, the phantom was placed on a glass slide, under which the Mn^{5+}, Nd^{3+} co-doped phosphor was placed (Fig. S10, ESI†).

The same measurements as described above were performed using a 1200 nm bandpass filter and a 1150 nm shortpass filter (Fig. S11, ESI†). In the case of the ink-free phantom, the intensity scale in which the two images are located differs significantly. Moreover, in the high temperature area, the intensity of the Mn^{5+} image decreased dramatically, while for the Nd^{3+} intensity image the values were similar throughout the measurement area. By diving the fluorescence images by each other, an LIR map was obtained, which clearly shows the temperature gradient (Fig. 5(b)). However, the range of LIR values for which the temperature gradient is observed remains around 0.3–0.7, which significantly deviates from the LIR range in which the temperature gradient was recorded in the absence of tissue phantoms (*i.e.*, LIR between ~0.8 and 1.1).

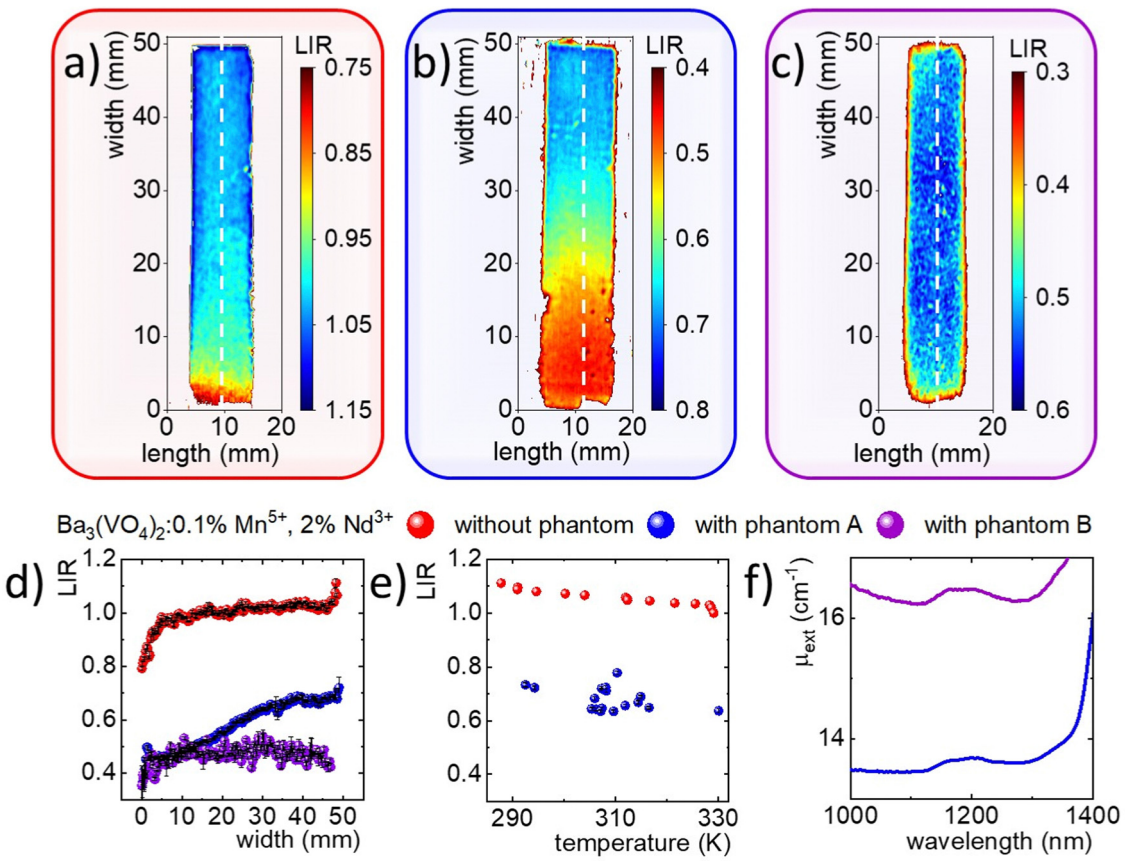

Fig. 5 LIR maps with the induced temperature gradient for $Ba_3(VO_4)_2$:0.1% Mn^{5+}, 2% Nd^{3+} phosphor without tissue phantoms (a), with tissue phantom A (b) and with tissue phantom B (c). Comparison of LIR values as the function of distance from the heating source (d). Comparison of the calibration curves of LIR *vs.* temperature for $Ba_3(VO_4)_2$:0.1% Mn^{5+}, 2% Nd^{3+} phosphor determined directly or through tissue phantom (e). Extinction coefficient as a function of wavelength for tissue phantoms A and B (f).

This indicates that the previously performed calibration curve recorded in the absence of the phantom is not appropriate and cannot be applied in this case. In addition, a similar experiment was performed using tissue phantom B (Fig. S12, ESI†), which also contained Indian ink. As shown in the filter images, in both cases, the temperature gradient is not distinguishable (Fig. S13, ESI†). This is also confirmed by the LIR maps, where the LIR values remain close to each other in the central part of the sample at around 0.6 (Fig. 5(c)).

To quantitatively compare the differences obtained from the three LIR maps, individual profiles marked as white dashed lines in Fig. 5(a)–(c), which are consistent with the direction in which the temperature gradient was generated, were selected and contrasted as a function of the distance from the heating element (Fig. 5(d)). The LIR profiles calculated for the cross-sections of samples with and without phantoms differ significantly.

Therefore, the luminescence thermometer was re-calibrated in the presence of tissue phantom A, acquiring luminescence images as a function of temperature while monitoring the temperature using the thermal camera. The so-acquired calibration curve was compared with the one determined for phosphor without optical obstructions (Fig. 5(e)). Unquestionably, the two calibration curves differ in the range of LIR values that cover the temperature range of 280 to 330 K. In addition, it can be found that due to the lower signal-to-noise ratio observed in this case the noisy character of the temperature profile when measured through tissue phantom A. Despite this, a linear function was determined that could serve as a calibration curve for the LIR vs temperature values. It resulted in the determination of a temperature map that confirms the temperature gradient obtained through tissue phantom A (Fig. S14, ESI†). Such a dramatic difference in the temperature readout of the same system with and without a tissue phantom forecloses the use of the ratiometric approach in bio-related thermal imaging unless specific actions are undertaken to obviate this limitation.[40] The effect described above is a consequence of the different extinction at different wavelengths and for different tissues. As it turns out in the example of tissue phantom A, the difference in LIR stems from the different value of μ_{ext} for the spectral ranges that covered the filters used in the experiment, *i.e.* μ_{ext} = 13.45 cm^{-1} and μ_{ext} = 13.65 cm^{-1} for wavelengths of 1070 nm and 1180 nm, respectively (Fig. 5(f)). On the other hand, tissue phantom B failed to register a temperature gradient, due to an excessively high extinction coefficient exceeding 16.0 cm^{-1} over the entire spectral range. This is a consequence of the high scattering coefficient, the increase of which plays a dominant role after the addition of Indian ink with carbon particles in relation to the absorption coefficient.

In conclusion, the developed Mn^{5+}/Nd^{3+} nanophosphor exhibits good performance for temperature sensing. However, in experiments conducted with tissue phantoms, it is evident that it cannot be immediately translated, as is in deep-tissue thermal imaging based on the LIR approach. This is due to the fact that the Mn^{5+} emission band partially overlaps with the absorption overtone of a water molecule. Conversely, the lifetime-based approach discussed in our previous work enables providing a reliable temperature readout even in deep tissue imaging. Therefore, the presented results confirm the superiority of the luminescence kinetics-based approach over the ratiometric approach for through-tissue thermal imaging.

Conclusions

In the present study, the thermometric properties of a ratiometric luminescence thermometer based on the emission intensity ratios of $^1E \rightarrow {}^3A_2$ of Mn^{5+} and $^4F_{3/2} \rightarrow {}^4I_{11/2}$ Nd^{3+} were analyzed as a function of Mn^{5+} and Nd^{3+} ion concentration. The emission intensity ratio of Mn^{5+} to Nd^{3+} ions due to inter-ionic energy transfer can be modulated by the concentration of Mn^{5+} ions. The difference in the electron configuration of the considered dopant ions generates a difference in the temperature quenching rate of their luminescence and thus makes it possible to use their LIR as a thermometric parameter. As the concentration of Nd^{3+} ions increased, the temperature range for which maximum sensitivities were recorded gradually decreased. Therefore, $Ba_3(VO_4)_2$:0.1% Mn^{5+}, 2% Nd^{3+} was chosen as the optimal temperature sensor in the physiological range. The confirmation of the application potential of the developed thermometer was provided by remote temperature measurements during laser-induced heating of the powder sample. However, the significant difference in extinction coefficients occurring at different measurement wavelengths in the case of thermal imaging using a tissue phantom showed that the described problems must be eliminated to increase the reliability of the measurement in such experiments. The presented work was focused on the fundamental studies of luminescence-based temperature imaging using $Ba_3(VO_4)_2$:0.1% Mn^{5+}, 2% Nd^{3+} and issues with a relatively wide particle size distribution and particle aggregation must be resolved before real applications. In addition, the influence of the bio-related medium on the luminescence response of this temperature sensor should be verified.

Conflicts of interest

There are no conflicts to declare.

Acknowledgements

W. M. P. acknowledges the financial support from the Bekker NAWA Programme BPN/BEK/2021/1/00029 funded by Polish National Agency for Academic Exchange. Additional funding was provided by the Spanish Ministerio de Ciencia e Innovación projects PID2019-106211RB-I00 and PID2020-118878RB-I00, the Instituto de Salud Carlos III (PI19/00565), the Comunidad Autónoma de Madrid project SI3/PJI/2021-00211 and network (S2022/BMD-7403 RENIM-CM), co-financed by the European structural and investment fund, and the Fundación para la Investigación Biomédica del Hospital Universitario Ramón y Cajal project IMP21_A4 (2021/0427), as well as COST action CA17140.

References

1 M. Kamimura, T. Matsumoto, S. Suyari, M. Umezawa and K. Soga, Ratiometric Near-Infrared Fluorescence Nanothermometry in the OTN-NIR (NIR II/III) Biological Window Based on Rare-Earth Doped β-$NaYF_4$ Nanoparticles, *J. Mater. Chem. B*, 2017, **5**(10), 1917–1925.

2 H. D. A. Santos, E. C. Ximendes, M. Iglesias-de la Cruz, C. del, I. Chaves-Coira, B. del Rosal, C. Jacinto, L. Monge, I. Rubia-Rodríguez, D. Ortega, S. Mateos, J. GarcíaSolé, D. Jaque and N. Fernández, *In Vivo* Early Tumor Detection and Diagnosis by Infrared Luminescence Transient Nanothermometry, *Adv. Funct. Mater.*, 2018, **28**(43), 1803924.

3 O. Savchuk, J. J. Carvajal, L. G. De la Cruz, P. Haro-González, M. Aguiló and F. Díaz, Luminescence Thermometry and Imaging in the Second Biological Window at High Penetration Depth with Nd:$KGd(WO_4)_2$ Nanoparticles, *J. Mater. Chem. C*, 2016, **4**(31), 7397–7405.

4 M. Jia, Z. Fu, G. Liu, Z. Sun, P. Li, A. Zhang, F. Lin, B. Hou and G. Chen, NIR-II/III Luminescence Ratiometric Nanothermometry with Phonon-Tuned Sensitivity, *Adv. Opt. Mater.*, 2020, **8**(6), 1901173.

5 S. Premcheska, M. Lederer and A. M. Kaczmarek, The Importance, Status, and Perspectives of Hybrid Lanthanide-Doped Upconversion Nanothermometers for Theranostics, *Chem. Commun.*, 2022, **58**(27), 4288–4307.

6 Z. Machala, M. Janda, K. Hensel, I. Jedlovský, L. Leštinská, V. Foltin, V. Martišovitš and M. Morvová, Emission Spectroscopy of Atmospheric Pressure Plasmas for Bio-Medical and Environmental Applications, *J. Mol. Spectrosc.*, 2007, **243**(2), 194–201.

7 E. Hemmer, P. Acosta-Mora, J. Méndez-Ramos and S. Fischer, Optical Nanoprobes for Biomedical Applications: Shining a Light on Upconverting and near-Infrared Emitting Nanoparticles for Imaging, Thermal Sensing, and Photodynamic Therapy, *J. Mater. Chem. B*, 2017, **5**(23), 4365–4392.

8 T. Togawa and H. Saito, Non-Contact Imaging of Thermal Properties of the Skin, *Physiol. Meas.*, 1994, **15**(3), 291–298.

9 D. Jaque and F. Vetrone, Luminescence Nanothermometry, *Nanoscale*, 2012, **4**(15), 4301–4326.

10 C. D. S. Brites, A. Millán and L. D. Carlos, Lanthanides in Luminescent Thermometry, in *Handbook on the Physics and Chemistry of Rare Earths*, ed. K. A. Gschneidner, J.-C. BŸnzli and V. Pecharsky, Elsevier, 2016, vol. 49, pp. 339–427.

11 M. D. Dramićanin, Sensing Temperature *via* Downshifting Emissions of Lanthanide-Doped Metal Oxides and Salts. A Review, *Methods Appl. Fluoresc.*, 2016, **4**(4), 42001.

12 A. Bednarkiewicz, L. Marciniak, L. D. Carlos and D. Jaque, Standardizing Luminescence Nanothermometry for Biomedical Applications, *Nanoscale*, 2020, **12**(27), 14405–14421.

13 M. Suta and A. Meijerink, A Theoretical Framework for Ratiometric Single Ion Luminescent Thermometers—Thermodynamic and Kinetic Guidelines for Optimized Performance, *Adv. Theory Simul.*, 2020, **3**(12), 2000176.

14 L. Marciniak, K. Kniec, K. Elżbieciak-Piecka, K. Trejgis, J. Stefanska and M. Dramićanin, Luminescence Thermometry with Transition Metal Ions. A Review, *Coord. Chem. Rev.*, 2022, **469**, 214671.

15 L. Marciniak, A. Bednarkiewicz, D. Kowalska and W. Strek, A New Generation of Highly Sensitive Luminescent Thermometers Operating in the Optical Window of Biological Tissues, *J. Mater. Chem. C*, 2016, **4**(24), 5559–5563.

16 L. Marciniak, A. Bednarkiewicz, J. Drabik, K. Trejgis and W. Strek, Optimization of Highly Sensitive YAG:Cr^{3+},Nd^{3+} Nanocrystal-Based Luminescent Thermometer Operating in an Optical Window of Biological Tissues, *Phys. Chem. Chem. Phys.*, 2017, **19**(10), 7343–7351.

17 W. Piotrowski, K. Trejgis, K. Maciejewska, K. Ledwa, B. Fond and L. Marciniak, Thermochromic Luminescent Nanomaterials Based on Mn^{4+}/Tb^{3+} Codoping for Temperature Imaging with Digital Cameras, *ACS Appl. Mater. Interfaces*, 2020, **12**(39), 44039–44048.

18 W. Liu, X. Wang, Q. Zhu and J. G. Li, Tb^{3+}/Mn^{2+} Singly/Doubly Doped $Sr_3Ce(PO_4)_3$ for Multi-Color Luminescence, Excellent Thermal Stability and High-Performance Optical Thermometry, *J. Alloys Compd.*, 2020, **829**, 154563.

19 G. Li, Y. Xue, Q. Mao, L. Pei, H. He, M. Liu, L. Chu and J. Zhong, Synergistic Luminescent Thermometer Using Co-Doped Ca_2GdSbO_6:Mn^{4+}/(Eu^{3+} or Sm^{3+}) Phosphors, *Dalt. Trans.*, 2022, **51**(12), 4685–4694.

20 D. Chen, W. Xu, S. Yuan, X. Li and J. Zhong, Ln^{3+}-Sensitized Mn^{4+} near-Infrared Upconverting Luminescence and Dual-Modal Temperature Sensing, *J. Mater. Chem. C*, 2017, **5**(37), 9619–9628.

21 J. Periša, Z. Ristić, V. Đorđević, M. Sekulić, T. Dramićanin, Ž. Antić and M. D. Dramićanin, Multiparametric Luminescence Thermometry from Dy^{3+}, Cr^{3+} Double Activated YAG, *J. Lumin.*, 2021, **238**, 118306.

22 In *Modern Luminescence Spectroscopy of Minerals and Materials. In Modern Luminescence Spectroscopy of Minerals and Materials*, ed. M. Gaft, R. Reisfeld and G. Panczer, Springer Berlin Heidelberg, Berlin, Heidelberg, 2005, pp. 11–34.

23 P. M. Gschwend, D. Niedbalka, L. R. H. Gerken, I. K. Herrmann and S. E. Pratsinis, Simultaneous Nanothermometry and Deep-Tissue Imaging, *Adv. Sci.*, 2020, **7**(12), 2000370.

24 M. D. Dramićanin, Ł. Marciniak, S. Kuzman, W. Piotrowski, Z. Ristić, J. Periša, I. Evans, J. Mitrić, V. Đorđević, N. Romčević, M. G. Brik and C. G. Ma, Mn^{5+}-Activated $Ca_6Ba(PO4)_4O$ near-Infrared Phosphor and Its Application in Luminescence Thermometry, *Light Sci. Appl.*, 2022, **11**(1), 279.

25 W. M. Piotrowski, R. Marin, M. Szymczak, E. Martín Rodríguez, D. H. Ortgies, P. Rodríguez-Sevilla, M. D. Dramićanin, D. Jaque and L. Marciniak, Mn^{5+} Lifetime-Based Thermal Imaging in the Optical Transparency Windows Through Skin-Mimicking Tissue Phantom, *Adv. Opt. Mater.*, 2022, 2202366.

26 J. A. Capobianco, G. Cormier, M. Bettinelli, R. Moncorgé and H. Manaa, Near-Infrared Intraconfigurational Luminescence

Spectroscopy of the Mn^{5+} ($3d^2$) Ion in Ca_2PO_4Cl, $Sr_5(PO_4)_3Cl$, Ca_2VO_4Cl and Sr_2VO_4Cl, *J. Lumin.*, 1992, **54**(1), 1–11.

27 Z. Ristić, W. Piotrowski, M. Medić, J. Periša, Ž. M. Antić, L. Marciniak and M. D. Dramićanin, Near-Infrared Luminescent Lifetime-Based Thermometry with Mn5+-Activated Sr3(PO4)2 and Ba3(PO4)2 Phosphors, *ACS Appl. Electron. Mater.*, 2022, **4**(3), 1057–1062.

28 M. P. Pechini Method of Preparing Lead and Alkaline Earth Titanates and Niobates and Coating Method Using the Same to Form a Capacitor, 1967.

29 D. Jaque, R. Marin, J. Yao, T. Muñoz-Ortiz, F. Sanz-Rodríguez, E. M. Rodríguez, D. H. Ortgies and J. G. Solé, Bismuth Selenide Nanostructured Clusters as Optical Coherence Tomography Contrast Agents: Beyond Gold-Based Particles, *ACS Photonics*, 2022, **9**(2), 559–566.

30 L. D. Merkle, A. Pinto, H. R. Verdún and B. McIntosh, Laser Action from Mn^{5+} in $Ba_3(VO_4)_2$, *Appl. Phys. Lett.*, 1992, **61**(20), 2386–2388.

31 P. Susse and M. J. Buerger, The Structure of $Ba_3(VO_4)_2$, *Z. Kristallogr. – Cryst. Mater.*, 1970, **131**(1–6), 161–174.

32 M. Azdouz, B. Manoun, R. Essehli, M. Azrour, L. Bih, S. Benmokhtar, A. A. Hou and P. Lazor, Crystal Chemistry, Rietveld Refinements and Raman Spectroscopy Studies of the New Solid Solution Series: $Ba_{3-x}Sr_x(VO_4)_2$ ($0 \leq x \leq 3$), *J. Alloys Compd.*, 2010, **498**(1), 42–51.

33 K. Cheng, C. Li, C. Yin, Y. Tang, Y. Sun and L. Fang, Effects of Sr^{2+} Substitution on the Crystal Structure, Raman Spectra, Bond Valence and Microwave Dielectric Properties of $Ba_{3-x}Sr_x(VO_4)_2$ Solid Solutions, *J. Eur. Ceram. Soc.*, 2019, **39**(13), 3738–3743.

34 K. C. Park and S. L. Mho, Photoluminescence Properties of $Ba_3V_2O_8$, $Ba_{3(1-x)}Eu_{2x}V_2O_8$ and $Ba_2Y_{2/3}V_2O_8$:Eu^{3+}, *J. Lumin.*, 2007, **122–123**(1–2), 95–98.

35 T. Senden, R. J. A. Van DIjk-Moes and A. Meijerink, Quenching of the Red Mn^{4+} Luminescence in Mn^{4+}-Doped Fluoride LED Phosphors, *Light Sci. Appl.*, 2018, **7**(1), 8.

36 B. Malysa, A. Meijerink and T. Jüstel, Temperature Dependent Luminescence Cr^{3+}-Doped $GdAl_3(BO_3)_4$ and $YAl_3(BO_3)_4$, *J. Lumin.*, 2016, **171**, 246–253.

37 M. Grinberg, $^2E \rightarrow {}^4A_2$ Fluorescence of Cr^{3+} in High and Intermediate Field Garnets, *J. Lumin.*, 1993, **54**(6), 369–382.

38 Z. Zhang, K. T. V. Grattan and A. W. Palmer, Temperature Dependences of Fluorescence Lifetimes in Cr^{3+}-Doped Insulating Crystals, *Phys. Rev. B: Condens. Matter Mater. Phys.*, 1993, **48**(11), 7772–7778.

39 K. Elzbieciak-Piecka, M. Suta and L. Marciniak, Structurally Induced Tuning of the Relative Sensitivity of $LaScO_3$:Cr^{3+} Luminescent Thermometers by Co-Doping Lanthanide Ions, *Chem. Eng. J.*, 2021, **421**, 129757.

40 Y. Shen, J. Lifante, N. Fernández, D. Jaque and E. Ximendes, In Vivo Spectral Distortions of Infrared Luminescent Nanothermometers Compromise Their Reliability, *ACS Nano*, 2020, **14**(4), 4122–4133.